WEARABLE ELECTRONICS

Flexible and stretchable power sources for wearable electronics

Alla M. Zamarayeva,[1] Aminy E. Ostfeld,[1] Michael Wang,[2] Jerica K. Duey,[1] Igal Deckman,[1] Balthazar P. Lechêne,[1] Greg Davies,[2] Daniel A. Steingart,[2] Ana Claudia Arias[1]*

Flexible and stretchable power sources represent a key technology for the realization of wearable electronics. Developing flexible and stretchable batteries with mechanical endurance that is on par with commercial standards and offer compliance while retaining safety remains a significant challenge. We present a unique approach that demonstrates mechanically robust, intrinsically safe silver-zinc batteries. This approach uses current collectors with enhanced mechanical design, such as helical springs and serpentines, as a structural support and backbone for all battery components. We show wire-shaped batteries based on helical band springs that are resilient to fatigue and retain electrochemical performance over 17,000 flexure cycles at a 0.5-cm bending radius. Serpentine-shaped batteries can be stretched with tunable degree and directionality while maintaining their specific capacity. Finally, the batteries are integrated, as a wearable device, with a photovoltaic module that enables recharging of the batteries.

INTRODUCTION

There is currently a great deal of interest in incorporating electronic functions into clothing and wearable devices for applications such as sensing and health care (*1*). Flexible and stretchable batteries play an important role in achieving the vision of wearable and conforming electronics. In recent years, several approaches have been developed to achieve compliant batteries. The initial demonstrations were flexible batteries based on conventional planar structures, assembled through stacking of the battery components (*2*, *3*). These designs evolved into more advanced form factors that enabled omnidirectional flexibility. Batteries in the shape of a fiber or wire (*4*–*17*), for example, can be twisted, tied, and woven into fabrics, allowing integration with wearable garments. In addition, several approaches to design stretchable batteries have been proposed, particularly using concepts of kirigami (*18*), origami (*19*), bridge-island battery design (*20*), arched electrode architecture (*21*), winding fibers around elastic support (*14*), embedding battery active materials within stretchable fabrics (*22*), and embedded nanowire elastic conductors (*23*). Despite innovative design strategies, there are no reports of wire batteries that exhibit fatigue resistance sufficient for applications in wearable systems that are likely to undergo thousands of flex cycles throughout their lifetime. In the case of stretchable batteries, none of the systems offer safety, compliance along multiple axes, and flexibility of electrode components simultaneously.

The compliant battery design concept introduced here addresses the aforementioned limitations of existing stretchable and wire-shaped battery systems. This strategy could be applied to a number of material composites and is demonstrated here on the silver-zinc (Ag-Zn) system, which has the advantage of high energy density combined with intrinsic safety. The core of the approach is in the utilization of metal current collectors with enhanced mechanical design, such as helical springs, serpentines, and spirals, as a structural support and backbone for the rest of the battery components. These architectures effectively accommodate stress imposed by mechanical deformation, thus minimizing strain experienced by the electrodes without compromising their surface area. Depending on the choice of current collector geometry, batteries can be fabricated with flexible or stretchable form factors to match the mechanical properties of wearable electronic systems while using the same battery chemistry, cell components, and fabrication steps.

We demonstrate the concept through fabrication and electrochemical-mechanical characterization of batteries with two form factors—flexible wire and stretchable serpentine. We achieve flexible wire batteries by shaping the current collector–electrode as a helical band spring. The wire batteries show linear capacity of 1.2 mA·hours cm^{-1}, are resilient to repetitive dynamic mechanical load, and can withstand >17,000 bending cycles to the bending radius of 0.5 cm under continuous operation mode without a decrease in electrochemical performance. Although using a current collector in the form of a helical band spring enabled omnidirectional flexibility of the battery, its elongation remained limited. Therefore, to achieve batteries that can be readily stretched, we used a current collector with serpentine ribbon geometry. In this structure, stretchability is facilitated by the out-of-plane rotations of serpentine ribbons, and batteries can operate under 100% stretch. The degree and direction of stretching can be modified by changing the serpentine geometry. In addition to stretching, the battery based on the serpentine ribbon can accommodate flexible motions in one plane. Thus, the omnidirectional, fatigue-resistant flexibility of the wire-shaped battery based on the helical band spring makes it the preferred geometry for flexible applications. On the other hand, the serpentine-shaped battery that can be readily stretched along two axes is preferred for integration with stretchable electronics.

Integrating compliant batteries with energy-harvesting devices is crucial for widespread realization of autonomous wearable power sources. Therefore, it is important not only to design batteries with compliant form factors but also to study their performance as a part of practical wearable systems. We explore a jewelry-integrated power source design in the form of a bracelet that includes a compliant battery and a photovoltaic module. The battery comprises part of the wristband that is expected to undergo flexing motions throughout the lifetime of the accessory. The battery with wire geometry is chosen because of its omnidirectional flexibility and resilience to flexing motions. However, if stretchability is one of the design considerations, then an accessory with the same energy-harvesting and storage capabilities can be achieved using a battery with serpentine architecture. The photovoltaic module

[1]Department of Electrical Engineering and Computer Sciences, University of California Berkeley, 508 Cory Hall, Berkeley, CA 94720, USA. [2]Mechanical and Aerospace Engineering, Andlinger Center for Energy and the Environment, Princeton University, D 428 Engineering Quadrangle, Princeton, NJ 08544, USA.
*Corresponding author. Email: acarias@eecs.berkeley.edu

charges the battery under multiple lighting conditions, including time-varying illumination that mimics the light conditions a wearable device may be exposed to during a typical daily routine. Such an accessory can harvest and store energy and provide power ranging from microwatts to milliwatts, depending on the illumination.

RESULTS

Design and fabrication of compliant batteries

The assembly process for wire- and serpentine-shaped batteries starts with the fabrication of a metal current collector of a specific geometry (ribbon or serpentine), followed by sequential deposition of the battery components. To scale the fabrication of wire or stretchable batteries to larger areas, the current collector must have good mechanical properties in addition to high conductivity. In our process, we use metal current collectors to achieve efficient current transport and use geometry to achieve flexibility. Typically, metal current collectors withstand elastic strains in a range of only 1% before plastic deformation and eventual fatigue. The geometry used here extends the range of elastic strain that the current collector can withstand during battery deformation. This contributes to an increase in fatigue resistance and battery lifetime. The extent of this increase is highly dependent on the current collector geometry. For example, in case of the serpentine current collector described in this work, the optically detectable plastic deformation does not occur until ~100% strain (fig. S1).

The fabrication process for the compliant batteries is presented in Fig. 1A. The mechanical properties of the final battery structure—wire (Fig. 1B) or serpentine (Fig. 1C) architecture—are determined by the current collector geometry. The helical band spring served as a current collector for the flexible wire–shaped batteries. To fabricate the helical band, we first cold-rolled the tin-coated copper wire by passing it between two rollers that compressed the cylindrical wire into 30-μm-thick and 400-μm-wide bands. Cold rolling served a dual function of fabricating bands with desired dimensions and increasing the yield point of the material. The resulting bands were wound into a helical spring shape with an inner diameter of 1 mm (fig. S2, A and B). Adjustments to geometric parameters, such as bandwidth–to–spring diameter ratio, inter-coil distance, and band thickness, can further decrease the stress: These parameters can be optimized to meet the geometric needs of the application, the energy density of the battery, and the flexibility requirement of the application. Analogously, the serpentine current collector for stretchable batteries was fabricated by bending the wire into the serpentine conformation and cold rolling it into ribbons (fig. S2, C and D). The serpentine ribbon current collector accommodates mechanical strain through out-of-plane rotations, thus reducing the stress placed on materials when the structure is stretched (*24*–*27*). Similarly to the spring, the dimensions of the serpentine can be tuned according to the deformability requirements of the application.

In our process, Zn was electroplated on the tin-coated copper current collector to form the battery anode. Copper was used as a current collector material because of its high ductility and resistance to corrosion in an alkaline environment. The ductility of copper allows the current collector to be cold-rolled into the desired shape and is not leveraged after that. Zn was plated at high current densities that resulted in hyperdendritic morphology. This morphology can accommodate mechanical stress more effectively than dense Zn because of the presence of void spaces between dendrites and has been shown recently to cycle at higher rates and with better consistency than standard particulate paste zinc anodes (*28*, *29*). The Zn–current collector composite was dip-coated in the polyvinyl alcohol (PVA)–based polymer electrolyte and wrapped with a cellophane layer. Cellophane protects the PVA separator and zinc anode from oxidation by silver ions. Cellophane membrane is an effective barrier for silver migration (*30*–*33*) because of the reducing properties of its constituent component—cellulose, which reduces silver ions to metallic silver, thus mitigating their further migration (*32*, *34*). The PVA polymer electrolyte further enhances the mechanical properties of the battery by providing flexible support to the Zn electrode and delocalizing the stress experienced by the electrode (*35*). Last, the Ag electrode was wrapped around the structure to finish the battery. The details of the battery components are demonstrated via scanning electron microscopy (SEM) characterization of the wire battery architecture (fig. S3). The silver electrode was constructed by embedding silver nanoparticle ink into a conductive thread and cold rolling the resulting composite to obtain a 30-μm-thick band (fig. S4). The

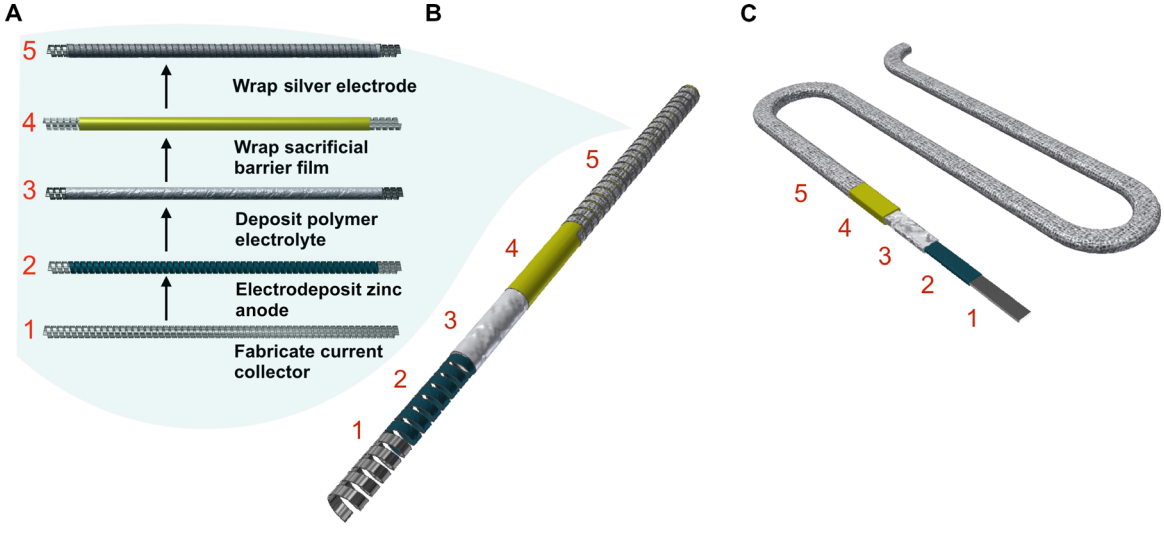

Fig. 1. Fabrication of the compliant batteries. (**A**) The assembly flow diagram for the (**B**) flexible wire–shaped batteries achieved by shaping the current collector–electrode as a helical band spring and (**C**) stretchable serpentine-shaped batteries fabricated using the current collector of serpentine ribbon geometry.

thread-embedded electrode used here can be easily wrapped around an electrode-electrolyte assembly of any shape, contributing to a simpler device manufacturing process. KOH (2 M)–ZnO (0.2 M) liquid electrolyte saturated with Bi_2O_3 was added in the amount of 50 μl per centimeter of battery length before sealing the battery. The Ag_2O cathode was electrochemically formed after the battery is fully assembled by a slow (0.05C) charging cycle to 1.8 V.

Electrochemical and mechanical performance of flexible wire batteries

The cycling performance of the wire battery, based on the helical band current collector, operated between 1.8 and 1.0 V, and corresponding charge-discharge curves are presented in Fig. 2 (A and B). The initial specific discharge capacity was approximately 1.33 mA·hours cm^{-1}, which fluctuated in the range of ~0.03 mA·hours cm^{-1} and stabilized after 33 electrochemical cycles. After 100 electrochemical cycles, the magnitude of the discharge capacity incrementally decreased and reached 1.25 mA·hours cm^{-1}. The reduction in the capacity was accompanied by a decrease of the voltage values of the discharge curve plateaus. The midpoint voltage of the discharge plateau decreased from ~1.52 V for the third electrochemical cycle to ~1.51 and ~1.48 V for the 30th and 90th electrochemical cycles, respectively, as shown in Fig. 2B. This behavior is anticipated in silver-zinc batteries and usually attributed to an increase in the impedance of the battery with cycling. This increase in impedance is caused by the deterioration of the polymer electrolyte and cellophane barrier by oxidative attacks of silver ions, loss of electrolyte through plastic encapsulation, and corrosion of the current collectors and electrodes (*32*). Overall, the battery charged at 0.25C and discharged at 0.5C rates has high specific capacity (~1.25 mA·hours cm^{-1} at 0.5C discharge rate) and exhibits stable performance with capacity retention of 94% over 100 electrochemical cycles. This is on the high end of performance of silver-zinc battery systems, which typically have had cycle lives limited to 50 to 100 electrochemical cycles (*34*).

Cycling performance of the battery at different rates (0.25C, 0.5C, C charge and 0.5C, C, 2C discharge, respectively) and corresponding charge-discharge curves are presented in Fig. 2C and Fig. 2D, respectively. The 2:1 ratio of discharge rate to charge rate was previously shown to be optimal because of the effects of cycling rate on the morphology of silver and on material utilization during cycling (*36*). The battery retained 96.5 and 82% of its capacity when the discharge rate was increased from 0.5C to C and from C to 2C, respectively. The specific capacity fluctuated in a range of ~0.025 mA·hours cm^{-1} when the battery was discharged at 0.5C and remained stable when the battery was discharged at C and 2C rates. The coulombic efficiency increased from ~95% at 0.5C to ~97 and ~98% at C and 2C rates, respectively. Typically, smaller Ag particles are formed when the battery is discharged at higher rates. Smaller particles are oxidized fully on the subsequent charge, resulting in a more efficient material utilization, whereas materials in larger particles (which form during slow discharge) can remain partially unused due to ionic transport limitations (*36*). Thus, the battery operates with higher efficiencies and improved stability when cycled at rates of 0.5C and above and retains 79% of its capacity when the discharge rate is increased from 0.5C to 2C.

Because power consumption of wearable electronic systems is application-dependent, the battery is likely to operate at varying discharge rates that are contingent on the load currents and duty cycle. We expect the battery to exhibit a stable cycling profile if the load currents fall between 0.5C and above. On the other hand, capacity might fluctuate or gradually fade with cycle number, if the battery is discharged at slower rates (*36*). However, among other factors, the period of time for which the slow discharge takes place determines whether a significant decrease or fluctuation in the battery capacity will occur. Because numerous wearable electronic systems operate in the high-current regime during data collection or transmission (*37*, *38*), the bulk of the battery's capacity is expected to discharge at high rates. Therefore, we do not expect a significant decrease in cycling stability when these batteries are used as part of wearable systems. The effect of the combination of charge/discharge rates on the capacity utilization of these batteries should be studied more rigorously with respect to specific applications.

Wire-shaped batteries for wearable applications are likely to undergo thousands of flex cycles of various combinations throughout their lifetime. Therefore, excellent mechanical endurance under repetitive load is a major design consideration for such a battery. The optical images of the flexible wire battery in flat and flexed configurations are presented in Fig. 2E and show high flexibility. The effect of repetitive dynamic mechanical load on the electrochemical performance was studied by monitoring the performance of the battery when the device is operated under continuous flexing conditions. The flexing was performed using a custom-made stage, shown in fig. S5, at the rate of two flexing cycles per minute. The length of the battery used for this study was 1.5 cm. By keeping the length of the battery comparable with the bending diameter, we ensured that the device was subjected to mechanical stress throughout its whole length. Figure 2F compares the cycling performance of the battery operated in a flat configuration and while being continuously flexed to a bending diameter of 1 cm. Minor fluctuations in capacity and decrease in efficiency are observed when the battery is operated in the continuous flexing regime versus when operated in a flat configuration. The capacity fluctuations were more pronounced during the first five electrochemical cycles, afterward the system stabilizes, as indicated by the constant capacity and the increased efficiency of consecutive cycles. The overall capacity of the battery increased by more than 10% as a result of flexing (fig. S6). Electrochemical impedance spectroscopy (EIS) measurements were carried out before and after flexing. The results and detailed analysis of the electromechanical characterization are presented in the Supplementary Methods and fig. S7. EIS measurements support the speculation that the increase in capacity is attributed to an increase in the active surface area of the limiting Ag electrode, leading to higher material utilization as a result of flexing (*39*–*45*). Thus, the electromechanical characterization demonstrated that constructing the battery around the helical band spring current collector resulted in a device resilient to repetitive dynamic mechanical load. The postmortem SEM characterization (fig. S8) suggests that efforts to further increase the robustness of the wire batteries should be focused on the polymer electrolyte.

Electrochemical and mechanical performance of stretchable batteries

The elongation of the battery based on the helical spring current collector is limited by the mechanical properties of the polymer electrolyte, cellophane layer, and silver electrode. Replacing the helical spring current collector with serpentine ribbon geometry overcomes this limitation and improves the effective macroscale elasticity of the battery.

The electromechanical characterization of serpentine-based batteries was performed using a simple structure. Before electrochemical characterization of the battery, the stretching and elastic deformation limits were determined empirically. The optical images for the serpentine ribbon current collectors stretched to various degrees and after releasing the stretch are presented in fig. S1. The serpentines had a

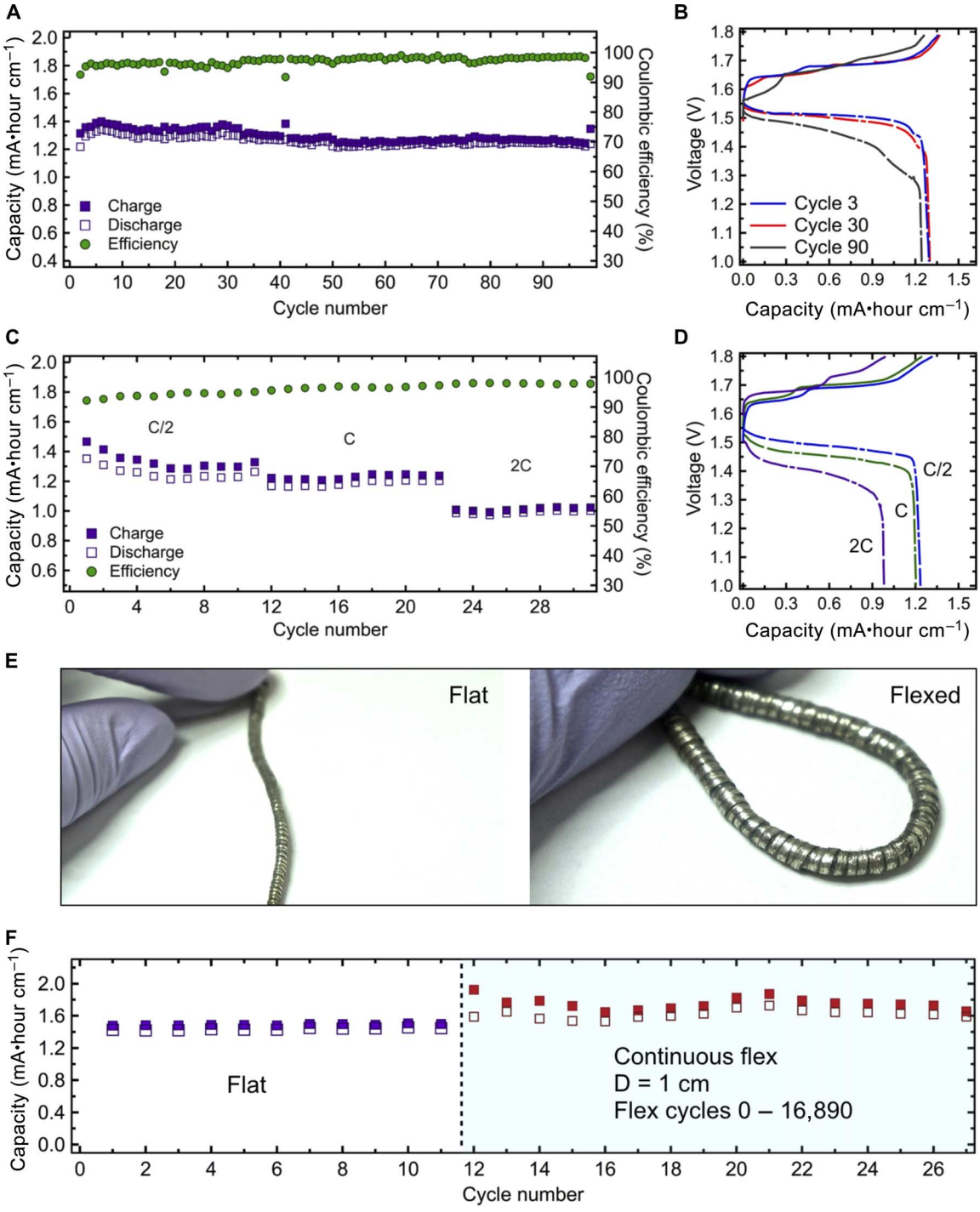

Fig. 2. Electrochemical and mechanical characterization of the flexible wire battery. (**A**) Capacity per unit length (mA·hour cm^{-1}) and coulombic efficiency (%) of silver-zinc wire battery cycled at 0.25C charge and 0.5C discharge rates between 1 and 1.8 V. (**B**) Galvanostatic charge-discharge curves for cycles 3, 30, and 90 of the battery in (A). (**C**) Specific capacity (mA·hour cm^{-1}) and coulombic efficiency (%) of silver-zinc wire battery cycled between 1 and 1.8 V at charge rates C, 0.5C, and 0.25C and discharge rates 2C, C, and 0.5C, respectively. (**D**) Galvanostatic charge-discharge curves of the battery in (C). (**E**) Optical images of the flexible wire battery in a relaxed and deformed state. (**F**) Cycling performance of the battery operated in a flat configuration and while being continuously flexed to a bending diameter (*D*) of 1 cm.

stretching limit close to 200%. Optically detectable plastic deformation occurred after 100% stretch. Although the current collectors are likely to deform plastically before reaching the 100% stretch limit (*27*), the deformation must have occurred locally, because the structure was able return to its original shape. Therefore, 100% stretch was chosen as the experimental limit for electromechanical testing of the battery.

The electromechanical performance of the serpentine battery was then evaluated by operating the battery flat, 100% stretched, and under

periodic stretch conditions at 0.25C charge and 0.5C discharge rates between 1 and 1.8 V. The specific capacity was normalized by the active area of the battery, that is, excluding the area occupied by the elastomer, and is in the range of 3.5 mA·hours cm^{-2} when discharged at the 0.5C rate, as can be seen in Fig. 3 (A to C). Figure 3A shows electrochemical cycling performance of the battery that was first operated in a relaxed configuration (region I) and then stretched to 100% (region II) followed by cycling in a relaxed configuration (region III). Subsequently, the battery was subjected to five sets of 100 stretch cycles. Every set of 100 stretch cycles was alternated with one electrochemical cycle (region IV) followed by cycling in a relaxed configuration (region V). This set of experiments allowed characterization of the electromechanical performance of the battery after periodic stretching as well as under the strain of 100%.

Electrochemical cycling performance of the battery in flat and 100% stretched configurations is presented in Fig. 3A as regions I, II, and III. The initial value of capacity is ~3.5 mA·hours cm^{-2}. The capacity increases during the electrochemical cycle immediately following the change in mechanical configuration of the battery, that is, after the battery is stretched (region II) and after it is released to its original state (region III), and then gradually stabilizes to its initial value during five consecutive cycles. The galvanostatic charge-discharge curves for the 2nd (flat configuration), 12th (stretched configuration), and 22nd (flat configuration) electrochemical cycles are presented in Fig. 3B. The internal resistance (IR) drop is not observed from the plateaus of the charge-discharge curves after the battery was stretched, indicating that active materials are not delaminating from the current collectors. Overall the battery exhibits stable performance in both flat and 100% stretched configurations with minor fluctuations in the capacity in both cases.

Region IV in Fig. 3A shows electrochemical cycling performance of the battery under the periodic stretch condition. The data demonstrate that the overall capacity of the battery increases by >3% after 200 stretch cycles and remains unaffected by 300 consecutive stretch cycles. This minor change in capacity can also be observed in the corresponding galvanostatic charge-discharge curves (for the electrochemical cycles following the 1st, 100th, 200th, 300th, 400th, and 500th stretch cycles) presented in Fig. 3C. The specific discharge capacity of the battery increased from ~3.5 to ~3.6 mA·hours cm^{-2} after 200 stretch cycles and remained stable on subsequent cycles. Thus, these results clearly demonstrate that the stretchable battery based on serpentine current collector exhibits stable cycling profile when tested under both periodic mechanical load conditions and in a stretched configuration.

The simple serpentine configuration is suitable for systems intended for uniaxial stretching. The configuration allows easy connection of several batteries in series to produce higher output voltage, if such is required. Four serpentine-shaped batteries are connected in series continuously to power an organic light-emitting diode (OLED) (with the current demand of 4.17 mA at ~6 V) while being stretched to 100%, as shown in Fig. 3D. Electronic systems designed for biaxial in-plane stretching cannot be effectively integrated with a battery having serpentine configuration because of the unidirectional stretchability of the serpentine system. This drawback can be overcome by changing the current collector geometry to a self-similar serpentine ribbon. Figure 3E shows schematics of the self-similar serpentine and optical images of the full battery assembled around such a current collector in relaxed and stretched configurations. Figure 3 shows that the geometry of the battery facilitates its biaxial stretching. This makes a battery with self-similar serpentine configuration a promising candidate for integration with devices that stretch along two axes.

Integration into wearable energy-harvesting and storage accessory

We have developed a wearable energy-harvesting and storage bracelet based on organic photovoltaic modules and the wire-shaped batteries described above. A power source in the form of a bracelet is ideal to power wearable sensors on the wrist, a location in which a number of vital biosignals can be measured (*1*). For this application, the battery dimensions are selected to provide sufficient capacity to power wearable low-power electronics, and the voltage of the photovoltaic module is selected to charge the battery directly without the addition of circuitry such as maximum power point tracking. The rate and efficiency of battery charging from the photovoltaic module are characterized under sunlight and indoor lighting conditions, and battery charging profiles through typical workday lighting conditions are studied.

The design of a battery for integration into a wearable system is guided by considerations such as safety, mechanical properties, and the amount of energy required to satisfy the application requirements. Wire architecture, whose design allows seamless integration into accessories, was chosen for this system. We used a low duty cycle resistive sensor system (*37*) as a target electronic system that could be powered by the battery. The battery was designed to meet the energy requirement of such a system, which was estimated to be ~6 megawatt-hours day^{-1}. The capacity of the wire battery can be readily adjusted by varying its length and was tuned to be 4 mA·hours, which is sufficient for powering the sensor system during the course of 1 day.

Because increasing the length of the wire battery can lead to increased IR, causing the battery to discharge at lower voltage, we investigated the magnitude of the voltage drop to ensure that the battery of the chosen length can meet the energy requirements of the target system and studied the cycling performance of the battery to ensure that it retains its capacity during cycling (Supplementary Methods and fig. S9). The battery maintained the capacity set by the wearable accessory design parameters after 50 electrochemical cycles, provided the target discharge voltage of ~1.5 V, and could be cycled at different charge-discharge rates in a range relevant to solar charging.

Although flexibility is frequently mentioned as a strict requirement for wearable electronics, jewelry is an exception because it often contains a combination of rigid and flexible structures. Thus, a wide range of potential jewelry-integrated power source designs can be explored that include both rigid and flexible devices. Here, rigid organic photovoltaic (OPV) modules were designed with the architecture shown in Fig. 4A, based on a bulk heterojunction active layer of poly[*N*-9′-heptadecanyl-2,7-carbazole-alt-5,5-(4,7-di-2-thienyl-2′,1′,3′-benzothiadiazole)] (PCDTBT) and [6,6]-phenyl C_{71}-butyric acid methyl ester ($PC_{71}BM$). The modules used indium tin oxide (ITO)–coated glass substrates, a hole transport layer of poly(3,4-ethylenedioxythiophene)/polystyrene sulfonate (PEDOT/PSS), and a cathode of aluminum with a dipole interlayer of polyethylenimine ethoxylated (PEIE). Glass substrates are an excellent barrier against oxygen and moisture permeation into the organic solar cell, in addition to withstanding the high temperatures required for deposition of high-quality ITO films (*46*). In addition, because wearable devices are expected to experience indoor light levels much of the time, the OPV modules were optimized for low light using the layer thicknesses reported previously (*47*).

When designing solar modules to be directly connected to batteries, the value of most interest is the power output over the battery voltage range during charging, which is ~1.6 to 1.8 V here. Figures S10 and S11 show the power output and the typical current-voltage characteristics of OPV modules with one to four series-connected cells under sunlight

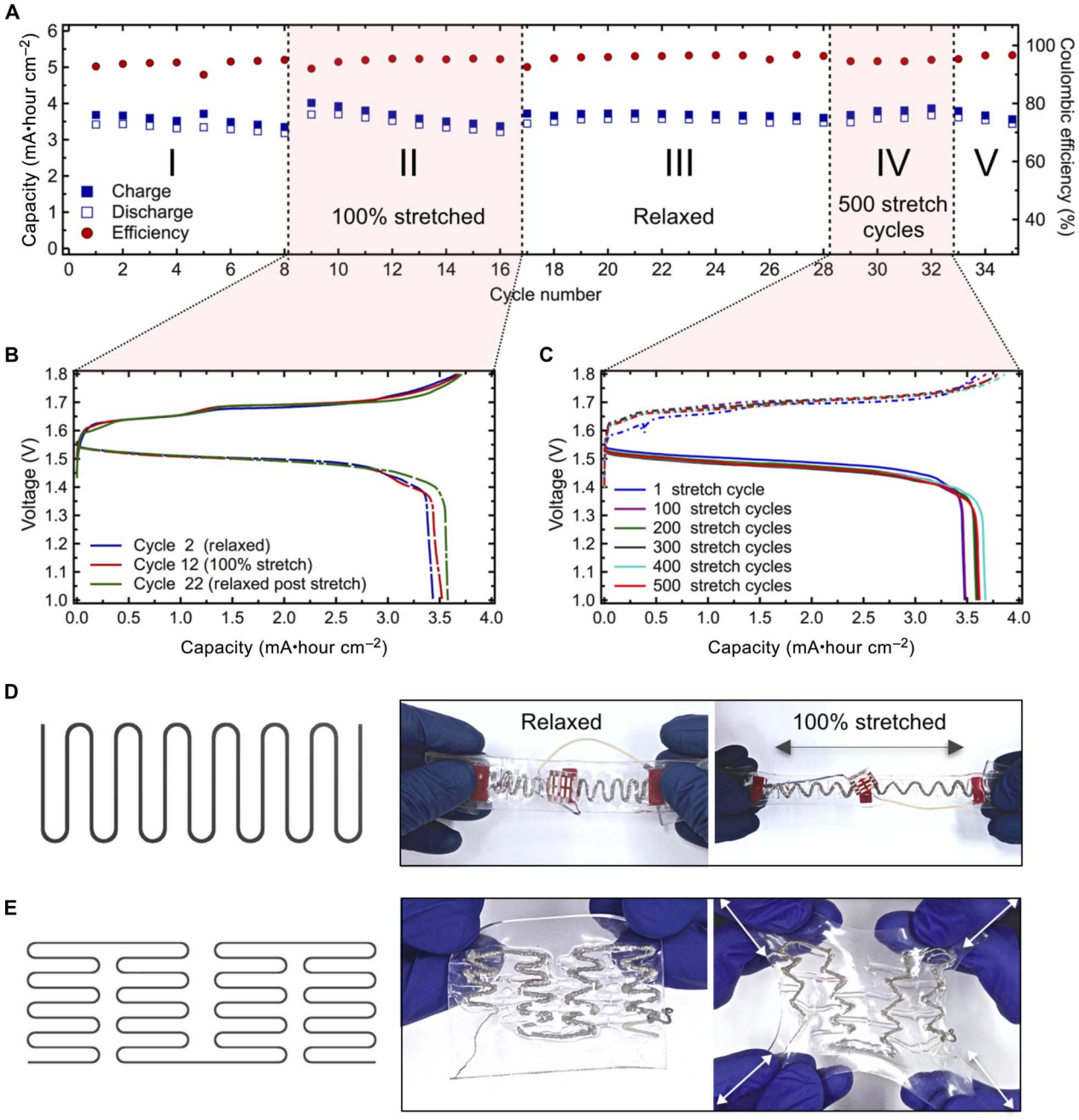

Fig. 3. Electrochemical and mechanical performance of the stretchable batteries. (**A**) Specific capacity (mA·hour cm^{-1}) and coulombic efficiency (%) of the battery that was first operated in a relaxed configuration (region I), stretched to 100% (region II) followed by cycling in a relaxed configuration (region III), and then subjected to five sets of 100 stretch cycles. Each set of 100 stretch cycles was alternated with one electrochemical cycle (region IV) followed by cycling in a relaxed configuration (region V). (**B**) Galvanostatic charge-discharge curves for the 2nd (flat configuration), 12th (stretched configuration), and 22nd (flat configuration) electrochemical cycles of the battery in (A). (**C**) Galvanostatic charge-discharge curves for the electrochemical cycles following the 1st, 100th, 200th, 300th, 400th, and 500th stretch cycles of the battery in (A). (**D**) Schematics of simple serpentine current collector and optical images of four serpentine-shaped batteries connected in series. Batteries continuously power an OLED while being subjected to uniaxial strain of 100%. (**E**) Schematics of self-similar serpentine current collector and optical images of the full battery assembled around such current collector. Geometry of the battery facilitates biaxial stretching.

and compact fluorescent light (CFL) lighting. A module with four cells was selected because it provides a constant and high charging current over the battery voltage range. Figure 4B and table S1 compare the output of the four-cell modules under CFL and LED illuminance of 300 lux, a typical lighting condition for offices and other indoor locations (*47*), and 3000 lux, corresponding to a location several centimeters below a typical indoor light source. Because the illuminance is weighted by the sensitivity of the human eye, light sources with the same illuminance (lux) but a different spectrum will provide a different irradiance (W m^{-2}). For example, the irradiance corresponding to an illuminance of 300 lux is 0.180 mW cm^{-2} for the CFL and 0.104 mW cm^{-2} for the LED. The CFL emission spectrum also has a greater overlap with the

absorption spectrum of the PCDTBT/$PC_{71}BM$ active layer than the LED does (*47*). The combination of these two factors resulted in a two times higher photocurrent and ~30% higher power conversion efficiency (PCE) under the CFL than under the LED.

The performance of the OPV module under simulated solar illumination is given in Fig. 4C. The efficiency was lower than with the CFL or LED lighting, 2.2%, in part because a smaller portion of the solar spectrum lies within the active layer's absorption window. The fill factor was reduced from >55 to 45% because of the increased impact of series resistance resulting from the higher current and particular module geometry. Nevertheless, the maximum power output under sunlight was 5 mW, which is sufficient to power many types of wearable health-monitoring systems (*37*, *48*, *49*).

The OPV modules and batteries were then connected together to characterize the solar charging process in a wearable energy-harvesting and storage system. Figure 4D shows photographs of a bracelet consisting of a four-cell OPV module with a wire battery integrated into the wristband, an example design of an energy-harvesting and storage accessory. The OPV module was connected directly to the battery, maintaining it at the same voltage as the battery throughout charging. The voltage across and current flowing into the battery during 12 hours of charging under the 3000 lux CFL are given in Fig. 4E, showing the increase in battery voltage as it charged as well as the stability of the OPV module current. Figure 4F shows the voltage and current as the battery was charged completely under simulated sunlight. The duration of the charge, 4 hours, with an average current of 1.4 mA, is consistent

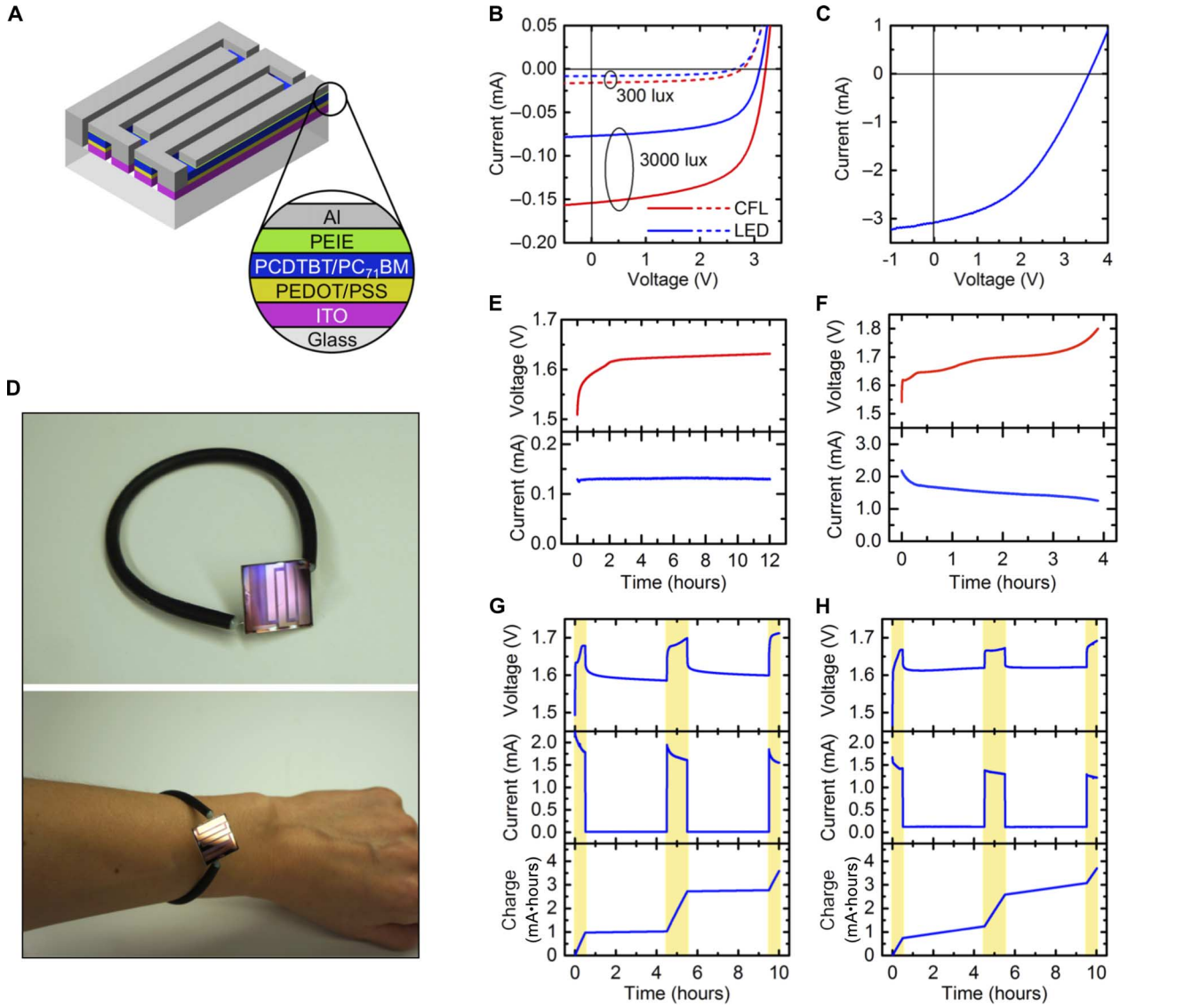

Fig. 4. Integrated energy-harvesting and storage system. (**A**) Structure of organic photovoltaic module. (**B** and **C**) Current-voltage characteristics of four-cell OPV module under various indoor lighting conditions (B) and sunlight (C). (**D**) Images of photovoltaic module and wire battery integrated into a wearable bracelet. (**E** and **F**) Voltage and current during battery charging. OPV module is exposed to either CFL lighting with illuminance of 3000 lux (E) or sunlight (F). (**G** and **H**) Voltage, current, and cumulative stored charge of solar battery charging during a simulated day of use. Yellow shaded areas indicate periods of exposure to sunlight. White areas correspond to CFL lighting with illuminance of 300 (G) or 3000 lux (H).

with the measured capacity of the battery operated at this rate. After each charging period, the battery was discharged at a current of 4 mA, and the energy transferred in each step of the energy conversion and storage process was calculated to determine the energy conversion and storage efficiency (ECSE), a figure of merit commonly used in solar supercapacitor charging systems (*50*). A full analysis of the ECSE calculation is given in the Supplementary Methods. The power conversion efficiency of the solar module was higher under the CFL than the sunlight, due to the better spectral overlap and reduced effect of series resistance, whereas the battery round-trip energy efficiency was higher under the sunlight because the faster charging rate creates a more optimal silver electrode morphology as discussed previously. Overall, the ECSE was 2.7 times higher under the CFL (2.7% versus 1.0% under sunlight).

To determine the relative contributions of indoor and outdoor light harvesting to the battery charge, the OPV modules were exposed to conditions simulating a typical day: 30 min of sunlight, 4 hours of indoor light, 1 hour of sunlight, 4 hours of indoor light, and 30 min of sunlight. The voltage and current into the battery were monitored throughout the day, using either 300 or 3000 lux CFL illumination for the indoor lighting condition, as shown in Fig. 4 (G and H, respectively). Figure 4 (G and H) also shows the cumulative stored charge in the battery, equal to the integral of the current. When the indoor illuminance is 300 lux, the amount of energy harvested is dominated by the amount of time spent in the sun. In the example day shown in Fig. 4G, only 2.8% of the charge stored in the battery resulted from the indoor light harvesting. However, when the indoor illuminance was increased to 3000 lux, the charge collected during the indoor portions of the day increased correspondingly by a factor of 10, contributing 27% of the total charge. The slopes of the stored charge curves in Fig. 4 (G and H) can be used to visualize the charge contributions during the different lighting phases, clearly indicating that the 3000 lux condition contributed a significant fraction of the total charge, whereas the 300 lux condition did not. Thus, if the system is expected to experience a lighting profile like that in Fig. 4G on most days, then having a high 1-sun ECSE is far more important than having a high low-light ECSE, because the charge collected during the indoor phases is nearly negligible compared to that of the sunlight phases. On the other hand, if the system will frequently be exposed to higher indoor illuminance, then a high low-light ECSE is also important because both sunlight and indoor phases would contribute significantly to the total charge. Because this system exhibits a particularly high ECSE under the CFL, it is especially well suited for wearing under conditions of higher indoor illuminance, such as those illustrated in Fig. 4H.

DISCUSSION

We demonstrate a new design concept to fabricate stretchable and flexible batteries. This strategy relies on using mechanically robust current collector geometries such as serpentines or helical springs to serve as a structural support for the rest of the battery components. The choice of current collector geometry determines the mechanical properties of the battery. To demonstrate the concept, we explored two different current collector geometries—helical band spring and serpentine ribbon. The battery fabricated around the helical band spring current collector has the form factor of a flexible wire. Such geometry ensured omnidirectional flexibility and fatigue resistance to flexing motions. Electrochemical-mechanical characterization of flexible wire–shaped batteries based on the helical band spring current collector showed that they can withstand flexing >17,000 times to the bending radius of 0.5 cm. The elongation of the wire battery is limited by the mechanical properties of the polymer electrolyte, cellophane layer, and silver electrode. To achieve devices that can be readily stretched, we fabricated batteries around serpentine ribbon current collectors. Serpentine-shaped batteries retained their electrochemical performance while being stretched to 100% and can accommodate flexible motions in one plane. Furthermore, we have shown that biaxial stretching can be realized by the utilization of a self-similar serpentine current collector. Therefore, using current collectors with spring and serpentine geometries as a backbone for the battery components represents a promising fabrication approach to compliant batteries with a range of mechanical properties. Integration with the organic solar module into a wearable energy bracelet and study of the performance of such an accessory under conditions simulating a day of use demonstrate the suitability of these batteries for real-life applications.

MATERIALS AND METHODS

Fabrication of battery components

To fabricate the helical band spring current collector, we used a 125-μm-diameter tin-coated copper wire (Alpha Wire, Tinned Copper, ASTMB-33, CID-A-A-59551). Tin (Sn), 40 micro-inches thick, is plated on copper by the manufacturer as a corrosion inhibitor. The wire was cold-rolled using calendar press to a thickness of 30 μm and winded around a 1-mm-diameter rod to form a helical band spring. To fabricate the serpentine current collector, the same wire was first bent into a serpentine structure of the desired configuration and then cold-rolled to a thickness of 30 μm.

The zinc electrode was electrodeposited on a tin-coated copper current collector (Alfa Aesar) in the galvanostatic mode at the current density of 40 mA cm^{-2} for 3000 s using Gamry potentiostat. To prepare the electrolyte, we dissolved corresponding amounts of KOH (Sigma-Aldrich, 85% anhydrous pellet) and ZnO (Sigma-Aldrich, 99.9%) in deionized (DI) water to produce 5.6 M KOH–0.37 M ZnO solution. Bi_2O_3 (0.1 g) (Sigma-Aldrich 99.999%) was added to the solution and mixed overnight.

The silver electrode was prepared by dipping stainless steel conductive thread (SparkFun, conductive thread #60) into silver nanoparticle ink (DuPont 5064H). Excess ink was thoroughly removed. The silver-coated thread was sintered for 30 min at 140°C in the vacuum oven. The resulting silver electrode was approximately 250 μm thick. The electrode was calendared to 20% of its original thickness using a calendar press.

Polymer electrolyte was prepared by mixing PVA (Sigma-Aldrich, M_W 85,000 to 124,000, 99% hydrolyzed) with DI water in a 1:10 ratio and left to dissolve overnight in the oven at 80°C. The liquid electrolyte was added to the mixture drop by drop to achieve a 1:1.3 PVA/KOH ratio (by dry weight). The mixture was stirred for at least 2 hours.

Battery assembly

Zn electrode was either dip-coated (in the case of the wire battery) or spray-coated (in the case of the serpentine battery) with PVA polymer electrolyte. The cellophane film (McMaster-Carr) was cut into strips and then wrapped around the anode-electrolyte assembly followed by wrapping the silver electrode. The batteries were sealed into stretchable elastomer (3M 4910). KOH (2 M)–ZnO (0.2 M) liquid electrolyte saturated with Bi_2O_3 was added before sealing the battery in the amount of 50 μl per centimeter of battery length. The serpentine battery was encapsulated within the elastomer matrix and sandwiched between

two elastomeric sheets. The matrix serves a dual function. First, it provides the spacing required for the out-of-plane rotation while the battery is being stretched. Second, it ensures that the battery deforms uniformly throughout the whole length. The schematic of the encapsulation is presented on the example of simple serpentine battery in fig. S12. The wire battery was encapsulated in a similar manner, with a well cut in the middle elastomer sheet replacing the matrix.

OPV module fabrication

ITO-coated glass substrates (Thin Film Devices) were cleaned in acetone followed by isopropanol and then plasma-cleaned for 5 min. PEDOT/PSS (Clevios P VP AI 4083) was spin-cast onto the ITO glass at 4000 rpm and baked on a hot plate at 130°C for 10 min. The active layer solution was made with 1:3.7 PCDTBT (Saint-Jean Photochimie)/$PC_{71}BM$ (Solaris), with total concentration of 21 mg/ml, in *o*-dichlorobenzene with 5% dimethyl sulfoxide. After heating overnight at 80°C to dissolve, the active layer solution was spin-cast in the glove box at 1250 rpm to form a film with thickness of 55 nm, as measured with a Dektak profilometer. PEIE (Sigma-Aldrich) diluted to 0.048 weight % (wt %) in ethanol was spin-cast onto the samples at 1250 rpm. Samples were then baked at 70°C for 10 min. The organic layers were mechanically scribed to allow series connections to be made between the cells. Aluminum (100 nm) was thermally evaporated to complete the modules. Modules were encapsulated using Delo Katiobond LP612 ultraviolet-curable epoxy and either glass or polyethylene naphthalate. The dimension of each cell was 1.5 × 0.2 cm, giving an active area of 0.3 cm^2. The size of the four-cell modules, including the active area of the cells, the spaces between them, and the contact areas, was 1.8 × 1.14 cm. Module efficiency was calculated on the basis of this area, 2.05 cm^2.

Battery characterization

EIS measurements were performed at frequencies ranging from 10^6 to 0.1 Hz at an amplitude of 10 mV at open circuit condition using Gamry Reference 600 electrochemical analyzer. The battery was fully discharged and allowed to equilibrate for at least 3 hours before each measurement. Full cells were tested using an MTI battery analyzer. SEM microscopy was carried out on TM-1000 (Hitachi).

OPV battery system characterization

Battery current collectors were connected to the corresponding OPV module terminals using conductive epoxy (Circuit Works, Technical Data Sheet #CW 2400). Simulated solar illumination (air mass 1.5) was provided using an Oriel Sol1A solar simulator. Indoor illumination was provided using either a CFL (GE Energy Smart Daylight CFL 6500 K) or a LED (Feit Electric Dimmable A19 LED 3000 K) bulb. The height of the bulbs above the solar module was adjusted to produce either 300 or 3000 lux, using a Hamamatsu S2387-66R silicon photodiode to measure the power and a Thorlabs CCS200 spectrophotometer to measure the lamp spectra. A Keithley 2400 Series SourceMeter was used to measure the current-voltage characteristics of the OPV modules and to record the current and voltage during solar battery charging.

SUPPLEMENTARY MATERIALS

Supplementary material for this article is available at http://advances.sciencemag.org/cgi/content/full/3/6/e1602051/DC1

fig. S1. The optical images for the serpentine ribbon current collectors stretched to 50, 100, 150, and 200% before and after releasing the stretch.

fig. S2. Dimensions and optical images of the helical band spring and serpentine ribbon current collectors.

fig. S3. SEM images of the wire battery components.

fig. S4. SEM characterization of the thread-embedded silver electrode.

fig. S5. The schematic of the custom-made flexing apparatus.

fig. S6. Charge-discharge curves of the wire battery operated under continuous flexing conditions.

fig. S7. Electrochemical cycling performance of the wire battery that was periodically stopped and flexed 1500 times in between the electrochemical cycles.

fig. S8. A postmortem analysis of the wire battery.

fig. S9. Performance characteristics of the 4-cm-long wire battery designed for integration with the solar module.

fig. S10. Performance characteristics of the OPV module designed for integration with the wire battery.

fig. S11. Power-voltage characteristics of the OPV module designed for integration with the wire battery.

fig. S12. The schematic of the encapsulation of serpentine battery.

fig. S13. Current-voltage characteristic of the particular OPV module used to charge the wire battery under sunlight.

table S1. Performance parameters of single-OPV cells and four-cell modules under various lighting conditions.

Supplementary Methods

REFERENCES AND NOTES

1. Y. Khan, A. E. Ostfeld, C. M. Lochner, A. Pierre, A. C. Arias, Monitoring of vital signs with flexible and wearable medical devices. *Adv. Mater.* **28**, 4373–4395 (2016).
2. L. Hu, H. Wu, F. La Mantia, Y. Yang, Y. Cui, Thin, flexible secondary Li-ion paper batteries. *ACS Nano* **4**, 5843–5848 (2010).
3. A. M. Gaikwad, G. L. Whiting, D. A. Steingart, A. C. Arias, Highly flexible, printed alkaline batteries based on mesh-embedded electrodes. *Adv. Mater.* **23**, 3251–3255 (2011).
4. J. Park, M. Park, G. Nam, J.-S. Lee, J. Cho, All-solid-state cable-type flexible zinc–air battery. *Adv. Mater.* **27**, 1396–1401 (2015).
5. W. Weng, Q. Sun, Y. Zhang, H. Lin, J. Ren, X. Lu, M. Wang, H. Peng, Winding aligned carbon nanotube composite yarns into coaxial fiber full batteries with high performances. *Nano Lett.* **14**, 3432–3438 (2014).
6. M. Peng, K. Yan, H. Hu, D. Shen, W. Song, D. Zou, Efficient fiber shaped zinc bromide batteries and dye sensitized solar cells for flexible power sources. *J. Mater. Chem. C* **3**, 2157–2165 (2015).
7. Y. H. Kwon, S.-W. Woo, H.-R. Jung, H. K. Yu, K. Kim, B. H. Oh, S. Ahn, S.-Y. Lee, S.-W. Song, J. Cho, H.-C. Shin, J. Y. Kim, Cable-type flexible lithium ion battery based on hollow multi-helix electrodes. *Adv. Mater.* **24**, 5192–5197 (2012).
8. H. Qu, O. Semenikhin, M. Skorobogatiy, Flexible fiber batteries for applications in smart textiles. *Smart Mater. Struct.* **24**, 025012 (2014).
9. T. Liu, Q.-C. Liu, J.-J. Xu, X.-B. Zhang, Cable-type water-survivable flexible Li-O_2 battery. *Small* **12**, 3101–3105 (2016).
10. M. Park, D.-S. Shin, J. Ryu, M. Choi, N. Park, S. Y. Hong, J. Cho, Organic-catholyte-containing flexible rechargeable lithium batteries. *Adv. Mater.* **27**, 5141–5146 (2015).
11. J. Ren, L. Li, C. Chen, X. Chen, Z. Cai, L. Qiu, Y. Wang, X. Zhu, H. Peng, Twisting carbon nanotube fibers for both wire-shaped micro-supercapacitor and micro-battery. *Adv. Mater.* **25**, 1155–1159 (2013).
12. J. Wang, C. Y. Wang, C. O. Too, G. G. Wallace, Highly-flexible fibre battery incorporating polypyrrole cathode and carbon nanotubes anode. *J. Power Sources* **161**, 1458–1462 (2006).
13. J.-K. Kim, J. Scheers, H.-S. Ryu, J.-H. Ahn, T.-H. Nam, K.-W. Kim, H.-J. Ahn, G.-B. Cho, P. Jacobsson, A layer-built rechargeable lithium ribbon-type battery for high energy density textile battery applications. *J. Mater. Chem. A* **2**, 1774–1780 (2014).
14. Y. Zhang, W. Bai, J. Ren, W. Weng, H. Lin, Z. Zhang, H. Peng, Super-stretchy lithium-ion battery based on carbon nanotube fiber. *J. Mater. Chem. A* **2**, 11054–11059 (2014).
15. Y. Xu, Y. Zhao, J. Ren, Y. Zhang, H. Peng, An all-solid-state fiber-shaped aluminum–air battery with flexibility, stretchability, and high electrochemical performance. *Angew. Chem. Int. Ed. Engl.* **55**, 7979–7982 (2016).
16. Y. Xu, Y. Zhang, Z. Guo, J. Ren, Y. Wang, H. Peng, Flexible, stretchable, and rechargeable fiber-shaped zinc–air battery based on cross-stacked carbon nanotube sheets. *Angew. Chem. Int. Ed. Engl.* **54**, 15390–15394 (2015).
17. X. Yu, Y. Fu, X. Cai, H. Kafafy, H. Wu, M. Peng, S. Hou, Z. Lv, S. Ye, D. Zou, Flexible fiber-type zinc-carbon battery based on carbon fiber electrodes. *Nano Energy* **2**, 1242–1248 (2013).
18. Z. Song, X. Wang, C. Lv, Y. An, M. Liang, T. Ma, D. He, Y.-J. Zheng, S.-Q. Huang, H. Yu, H. Jiang, Kirigami-based stretchable lithium-ion batteries. *Sci. Rep.* **5**, 10988 (2015).
19. Z. Song, T. Ma, R. Tang, Q. Cheng, X. Wang, D. Krishnaraju, R. Panat, C. K. Chan, H. Yu, H. Jiang, Origami lithium-ion batteries. *Nat. Commun.* **5**, 3140 (2014).
20. S. Xu, Y. Zhang, J. Cho, J. Lee, X. Huang, L. Jia, J. A. Fan, Y. Su, J. Su, H. Zhang, H. Cheng, B. Lu, C. Yu, C. Chuang, T.-I. Kim, T. Song, K. Shigeta, S. Kang, C. Dagdeviren, I. Petrov, P. V. Braun, Y. Huang, U. Paik, J. A. Rogers, Stretchable batteries with self-similar

serpentine interconnects and integrated wireless recharging systems. *Nat. Commun.* **4**, 1543 (2013).
21. W. Weng, Q. Sun, Y. Zhang, S. He, Q. Wu, J. Deng, X. Fang, G. Guan, J. Ren, H. Peng, A gum-like lithium-ion battery based on a novel arched structure. *Adv. Mater.* **27**, 1363–1369 (2015).
22. A. M. Gaikwad, A. M. Zamarayeva, J. Rousseau, H. Chu, I. Derin, D. A. Steingart, Highly stretchable alkaline batteries based on an embedded conductive fabric. *Adv. Mater.* **24**, 5071–5076 (2012).
23. C. Yan, X. Wang, M. Cui, J. Wang, W. Kang, C. Y. Foo, P. See Lee, Stretchable silver-zinc batteries based on embedded nanowire elastic conductors. *Adv. Energy Mater.* **4**, 1–6 (2014).
24. Y. Zhang, S. Xu, H. Fu, J. Lee, J. Su, K.-C. Hwang, J. A. Rogers, Y. Huang, Buckling in serpentine microstructures and applications in elastomer-supported ultra-stretchable electronics with high areal coverage. *Soft Matter* **9**, 8062–8070 (2013).
25. Y. Zhang, H. Fu, Y. Su, S. Xu, H. Cheng, J. A. Fan, K.-C. Hwang, J. A. Rogers, Y. Huang, Mechanics of ultra-stretchable self-similar serpentine interconnects. *Acta Mater.* **61**, 7816–7827 (2013).
26. Y. Zhang, S. Wang, X. Li, J. A. Fan, S. Xu, Y. M. Song, K.-J. Choi, W.-H. Yeo, W. Lee, S. N. Nazaar, B. Lu, L. Yin, K.-C. Hwang, J. A. Rogers, Y. Huang, Experimental and theoretical studies of serpentine microstructures bonded to prestrained elastomers for stretchable electronics. *Adv. Funct. Mater.* **24**, 2028–2037 (2014).
27. C. Lv, H. Yu, H. Jiang, Archimedean spiral design for extremely stretchable interconnects. *Extreme Mech. Lett.* **1**, 29–34 (2014).
28. T. Gupta, A. Kim, S. Phadke, S. Biswas, T. Luong, B. J. Hertzberg, M. Chamoun, K. Evans-Lutterodt, D. A. Steingart, Improving the cycle life of a high-rate, high-potential aqueous dual-ion battery using hyper-dendritic zinc and copper hexacyanoferrate. *J. Power Sources* **305**, 22–29 (2016).
29. M. Chamoun, B. J. Hertzberg, T. Gupta, D. Davies, S. Bhadra, B. Van Tassell, C. Erdonmez, D. A. Steingart, Hyper-dendritic nanoporous zinc foam anodes. *NPG Asia Mater.* **7**, e178 (2015).
30. H. L. Lewis, S. P. Wharton, Zinc and silver migration during rechargeable silver-zinc cell cycling, paper presented at the 12th Annual Battery Conference on Applications and Advances, Long Beach, CA, 14 to 17 January 1997.
31. P. Arora, Z. J. Zhang, Battery separators. *Chem. Rev.* **104**, 4419–4462 (2004).
32. D. Linden, *Handbook of Batteries* (McGraw-Hill, 2004).
33. A. Himy, "Separators for high-rate, non-reserve zinc-silver oxide batteries" (Technical Report ECOM-0310-1, 1967); http://oai.dtic.mil/oai/oai?verb=getRecord&metadataPrefix=html&identifier=AD0665631.
34. A. P. Karpinski, B. Makovetski, S. J. Russell, J. R. Serenyi, D. C. Williams, Silver–zinc: Status of technology and applications. *J. Power Sources* **80**, 53–60 (1999).
35. Z. Suo, Mechanics of stretchable electronics and soft machines. *MRS Bull.* **37**, 218–225 (2012).
36. A. M. Zamarayeva, A. M. Gaikwad, I. Deckman, M. Wang, B. Khau, D. A. Steingart, A. C. Arias, Fabrication of a high-performance flexible silver-zinc wire battery. *Adv. Electron. Mater.* **2**, 1500296 (2016).
37. J. D. MacKenzie, C. Ho, Perspectives on energy storage for flexible electronic systems. *Proc. IEEE* **103**, 535–553 (2015).
38. A. E. Ostfeld, A. M. Gaikwad, Y. Khan, A. C. Arias, High-performance flexible energy storage and harvesting system for wearable electronics. *Sci. Rep.* **6**, 26122 (2016).
39. P. Suresh, D. H. Nagaraju, A. K. Shukla, N. Munichandraiah, Analysis of ac impedance of AgO-Zn cells: Effects of state-of-charge, temperature and cycle-life. *Electrochim. Acta* **50**, 3262–3272 (2005).
40. J.-P. Randin, Determination of state-of-discharge of zinc-silver oxide button cells. III. In situ impedance measurements of each electrode. *J. Appl. Electrochem.* **15**, 591–601 (1985).
41. K. T. Braam, S. K. Volkman, V. Subramanian, Characterization and optimization of a printed, primary silver–zinc battery. *J. Power Sources* **199**, 367–372 (2012).
42. S. Devan, V. R. Subramanian, R. E. White, Analytical solution for the impedance of a porous electrode. *J. Electrochem. Soc.* **151**, A905–A913 (2004).
43. T. P. Dirkse, A potentiostatic study of the electrolytic formation of AgO. *Electrochim. Acta* **35**, 1445–1449 (1989).
44. C. P. Wales, The microstructure of sintered silver electrodes. *J. Electrochem. Soc.* **118**, 1021–1026 (1971).
45. A. M. Gaikwad, J. W. Gallaway, D. Desai, D. A. Steingart, Electrochemical-mechanical analysis of printed silver electrodes in a microfluidic device. *J. Electrochem. Soc.* **158**, A154–A162 (2011).
46. C. Lungenschmied, G. Dennler, H. Neugebauer, S. N. Sariciftci, M. Glatthaar, T. Meyer, A. Meyer, Flexible, long-lived, large-area, organic solar cells. *Sol. Energy Mater. Sol. Cells* **91**, 379–384 (2007).
47. B. P. Lechêne, M. Cowell, A. Pierre, J. W. Evans, P. K. Wright, A. C. Arias, Organic solar cells and fully printed super-capacitors optimized for indoor light energy harvesting. *Nano Energy* **26**, 631–640 (2016).
48. M. Van Bavel, V. Leonov, R. F. Yazicioglu, T. Torfs, C. Van Hoof, N. E. Posthuma, R. J. M. Vullers, Wearable battery-free wireless 2-channel EEG systems powered by energy scavengers. *Sens. Transducers J.* **94**, 103–115 (2008).
49. V. Misra, A. Bozkurt, B. Calhoun, T. Jackson, J. Jur, J. Lach, B. Lee, J. Muth, O. Oralkan, M. Ozturk, S. Trolier-Mckinstry, D. Vashaee, D. Wentzloff, Y. Zhu, Flexible technologies for self-powered wearable health and environmental sensing. *Proc. IEEE* **103**, 665–681 (2015).
50. D. Schmidt, M. D. Hager, U. S. Schubert, Photo-rechargeable electric energy storage systems. *Adv. Energy Mater.* **6**, 1500369 (2016).

Acknowledgments: We thank P. Wright for granting access to his laboratory, A. Gaikwad for constructive discussions, and C. Lochner for providing OLED. **Funding:** This work is based on work supported in part by the NSF under Cooperative Agreement no. EEC-1160494 and by the NSF Graduate Research Fellowships Program under grant no. DGE-1106400.
Author contributions: A.M.Z., M.W., I.D., G.D., D.A.S., and A.C.A. designed the batteries and the experiments for the battery characterization. A.M.Z., M.W., and G.D. fabricated the batteries and carried out the experiments for their characterization. A.E.O., B.P.L., A.M.Z., and A.C.A. designed experiments for the integrated energy-harvesting and storage system. A.E.O. and J.K.D. fabricated and characterized solar modules for the integrated system. A.M.Z. fabricated and characterized batteries for the integrated system. A.E.O. carried out experiments for the performance of the integrated system. A.M.Z., A.E.O., D.A.S., and A.C.A. wrote the manuscript. All authors commented on the manuscript. **Competing interests:** The authors declare that they have no competing interests. **Data and materials availability:** All data needed to evaluate the conclusions in the paper are present in the paper and/or the Supplementary Materials. Additional data related to this paper may be requested from the authors.

Submitted 28 August 2016
Accepted 28 April 2017
Published 16 June 2017
10.1126/sciadv.1602051

Citation: A. M. Zamarayeva, A. E. Ostfeld, M. Wang, J. K. Duey, I. Deckman, B. P. Lechêne, G. Davies, D. A. Steingart, A. C. Arias, Flexible and stretchable power sources for wearable electronics. *Sci. Adv.* **3**, e1602051 (2017).